

Direct Observation of Quadrupolar Strain Fields forming a Shear Band in Metallic Glasses

Sangjun Kang, Di Wang, Arnaud Caron, Christian Minnert, Karsten Durst, Christian Kübel,* and Xiaoke Mu*

For decades, scanning/transmission electron microscopy (S/TEM) techniques have been employed to analyze shear bands in metallic glasses and understand their formation in order to improve the mechanical properties of metallic glasses. However, due to a lack of direct information in reciprocal space, conventional S/TEM cannot characterize the local strain and atomic structure of amorphous materials, which are key to describe the deformation of glasses. For this work, 4-dimensional-STEM (4D-STEM) is applied to map and directly correlate the local strain and the atomic structure at the nanometer scale in deformed metallic glasses. Residual strain fields are observed with quadrupolar symmetry concentrated at dilated Eshelby inclusions. The strain fields percolate in a vortex-like manner building up the shear band. This provides a new understanding of the formation of shear bands in metallic glass.

1. Introduction

Metallic glasses are amorphous metallic alloys. They possess significantly higher elasticity and yield strength compared to their crystalline counterparts and have attracted a lot of interest as potential engineering materials.^[1–2] However, metallic glasses yield abruptly when high stresses are applied with the plastic deformation locally concentrated in narrow nanoscale regions, giving rise to the formation of shear bands.^[3–4] Catastrophic shear banding strongly limits the fracture toughness of metallic glasses and impedes their widespread application.

Atomic-level simulations, which can numerically inspect the strain evolution

and local atomic rearrangement in cubes with dimensions of a few tens of nanometers and over time scales of nanoseconds at a high deformation rate, have been employed extensively to study the shear banding process.^[5–9] Experimentally, only a few electron microscopy and atomic probe tomography investigations, which provide the spatial resolution necessary for resolving nanoscale features, have been devoted to directly investigate the structure and chemistry of individual shear bands.^[10–14]

Using scanning transmission electron microscopy (STEM) annular dark field (ADF) imaging, Maaß et al. observed a reduction in scattering power at the core of shear bands suggesting spatially localized free volume,^[10] while Rösner et al. observed alternating scattering power along shear bands, which have been associated with local density fluctuations.^[11,12] Chen et al.^[15] and Yan et al.^[16] showed nanocrystallization after shear banding of metallic glasses by high-resolution TEM. The observations provide detailed views of the shear band morphology. However, conventional S/TEM imaging techniques cannot provide concrete information on the atomic structure of amorphous materials due to the lack of direct information in real or reciprocal space. A solution has been to directly investigate electron diffraction patterns acquired from a nano volume using a focused electron beam, e.g., nano-beam electron diffraction (NBD),^[17–19] and fluctuation electron microscopy (FEM).^[12,20] These studies reveal local structural variation from icosahedral to tetragonal atomic packing in metallic glasses and a structural fluctuation of the medium-range order (MRO) within shear bands. The measurements require an extremely thin specimen (ideally a few tens of atomic layers) to prevent plural scattering and significant overlap of features in the projected diffraction patterns. This gives rise to difficulty for

S. Kang, D. Wang, C. Kübel, X. Mu
Institute of Nanotechnology (INT)
Karlsruhe Institute of Technology (KIT)
76344 Eggenstein-Leopoldshafen, Germany
E-mail: christian.kuebel@kit.edu; xiaoke.mu@kit.edu


S. Kang, C. Kübel
Joint Research Laboratory Nanomaterials
Technical University of Darmstadt (TUDa)
64287 Darmstadt, Germany

S. Kang
Advanced Analysis Center
Korea Institute of Science and Technology (KIST)
Seoul 02792, Republic of Korea

D. Wang, C. Kübel
Karlsruhe Nano Micro Facility (KNMFi)
Karlsruhe Institute of Technology (KIT)
76344 Eggenstein-Leopoldshafen, Germany

A. Caron
Korea University of Technology and Education (Koreatech)
Cheonan 330708, Republic of Korea

C. Minnert, K. Durst
Physical Metallurgy
Department of Materials Science
Technical University of Darmstadt (TUDa)
64287 Darmstadt, Germany

 The ORCID identification number(s) for the author(s) of this article can be found under <https://doi.org/10.1002/adma.202212086>

© 2023 The Authors. Advanced Materials published by Wiley-VCH GmbH. This is an open access article under the terms of the Creative Commons Attribution-NonCommercial License, which permits use, distribution and reproduction in any medium, provided the original work is properly cited and is not used for commercial purposes.

DOI: 10.1002/adma.202212086

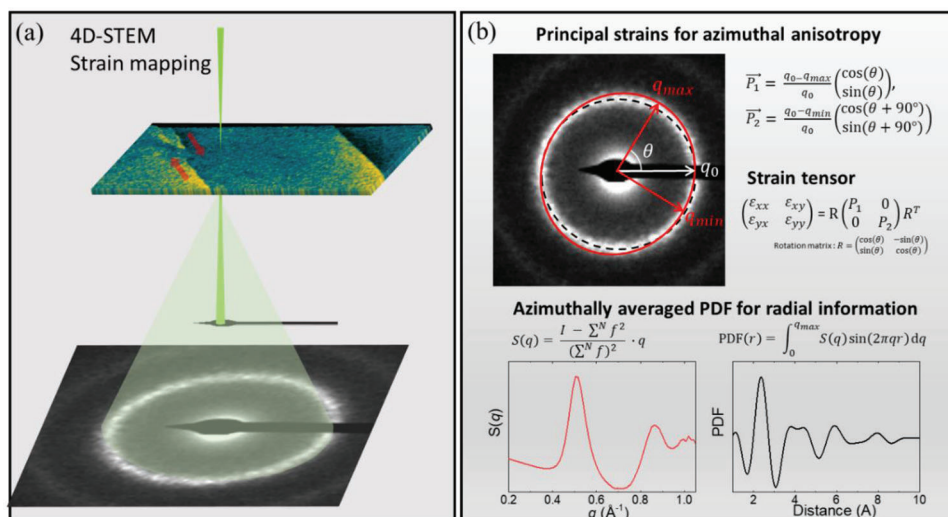


Figure 1. Schematic illustration of 4D-STEM based strain and PDF mapping. a) The quasi-parallel electron probe is focused on the TEM lamella. Spatially-resolved diffraction patterns are recorded by a camera during stepwise scanning of the probe over the area of interest. b) Data processing: principal strains (\vec{P}_1 and \vec{P}_2) are calculated from the elliptical distortion of the diffraction ring. For better visualization, the diffraction pattern is elongated along the principal direction. The strain tensors are algebraically obtained by projecting the principal strains to the reference coordinate system (x - and y -axis). For PDF analysis, the local diffraction patterns are azimuthally integrated into intensity profiles $I(q)$. Structure factors, $S(q)$, are obtained by background subtraction of $I(q)$. The PDFs are obtained by Fourier sine transformation of $S(q)$ as described in.^[21,22]

experimentally investigating highly strained samples with shear bands, in which residual stresses are an important aspect of the deformed glass, which can relax during the sample thinning process with the increased surface-to-volume ratio.

For this work, we used 4D-STEM to simultaneously map the local strain and the atomic structure via pair distribution function (PDF) analysis in thick metallic glasses (≈ 200 nm). The measurement suffers limited nonlinear degradation from the plural scattering due to the almost isotropic amorphous structure averaged at the nanometers scale. Therefore, this approach is fairly robust against sample thickness. We correlate the residual strain field and atomic structure at the nanoscale to investigate the shear band structure and formation mechanisms.

Figure 1a schematically shows the 4D-STEM setup. A quasi-parallel electron probe is focused to ≈ 5 nm diameter on an electron transparent sample. 4D-STEM records 2D images of local diffraction patterns over a 2D grid of each probe position by stepwise scanning of the probe over the area of interest. Diffraction patterns of metallic glasses are characterized by a set of diffuse diffraction rings due to their amorphous atomic arrangement. The 2D patterns contain azimuthal and radial information. Stress distorts the atomic structure and introduces an anisotropy resulting in an azimuthally elliptical distortion of the diffraction ring. Poulsen et al.^[23] and Gammer et al.^[24] demonstrated the measurement of the local elastic strain of amorphous materials by quantifying the elliptical deviation present in each diffraction pattern. In this study, we further developed this approach. We obtain the principal strains from the long and short axes of the ellipse indicated by q_{\max} and q_{\min} . The strain tensor is obtained by algebraic transformation of the principal strains to the loading coordinates. We quantify the deviatoric and volumetric strain from the principal strains to disentangle the true local distortion of the material and the local net volume change due to hydrostatic stresses. Moreover, a PDF analysis is performed as a structural

descriptor based on the 4D-STEM dataset to analyze the local atomic structure of metallic glasses following the STEM-PDF method described by Mu et al.^[21,22] One can, in principle, analyze the PDF at each azimuthal angle of the diffraction patterns due to the anisotropic distortion in regions with large deviatoric strain.^[23,25] In this work, we average the diffraction pattern azimuthally to reach the necessary signal quality for the PDF analysis. The obtained PDFs provide information on atomic configurations in the probed nano volume. We analyze the nearest atomic distances by fitting a Gaussian peak to the 1st peak of the PDF (i.e., the radius of the 1st coordination shell). The 4D-STEM approach, therefore, provides a correlative visualization of the nanoscale strain field and the atomic structure information.

We used a $\text{Fe}_{85.2}\text{Si}_{0.5}\text{B}_{9.5}\text{P}_4\text{Cu}_{0.8}$ (at.%) metallic glass ribbon as an example in this study, which receives attention owing to its soft ferromagnetism.^[26] The metallic glass was deformed by scratch testing at ambient conditions using a diamond tip. As a result, shear offsets occurred on the scratched surface. A TEM lamella including the shear offsets, as shown in a shadowed rectangle in **Figure 2a**, was lifted out by a focused ion beam (FIB) system and thinned to a thickness of ≈ 200 nm to balance electron transparency and prevent strain relaxation due to the increased surface-to-volume ratio during thinning (Figure S1, Supporting Information). **Figure 2b** shows a HAADF-STEM image of a TEM lamella, where the locations of shear bands are estimated based on the shear offset at the surface (red dashed lines). We acquired a 4D-STEM map at the area indicated by the black rectangle with a step size of 5.8 nm, including the shear bands of interest labeled SB1 and SB2.

Figure 2c shows a map of the volumetric strain (ϵ_{Vol}). **Figure 2d** visualizes the maximum shear strain (γ_{\max}). The amplitude of the field (brightness) is defined by the strength of the deviatoric strain. The orientation of the field (colors) follows the orientation of maximum tensile strain. γ_{\max} provides

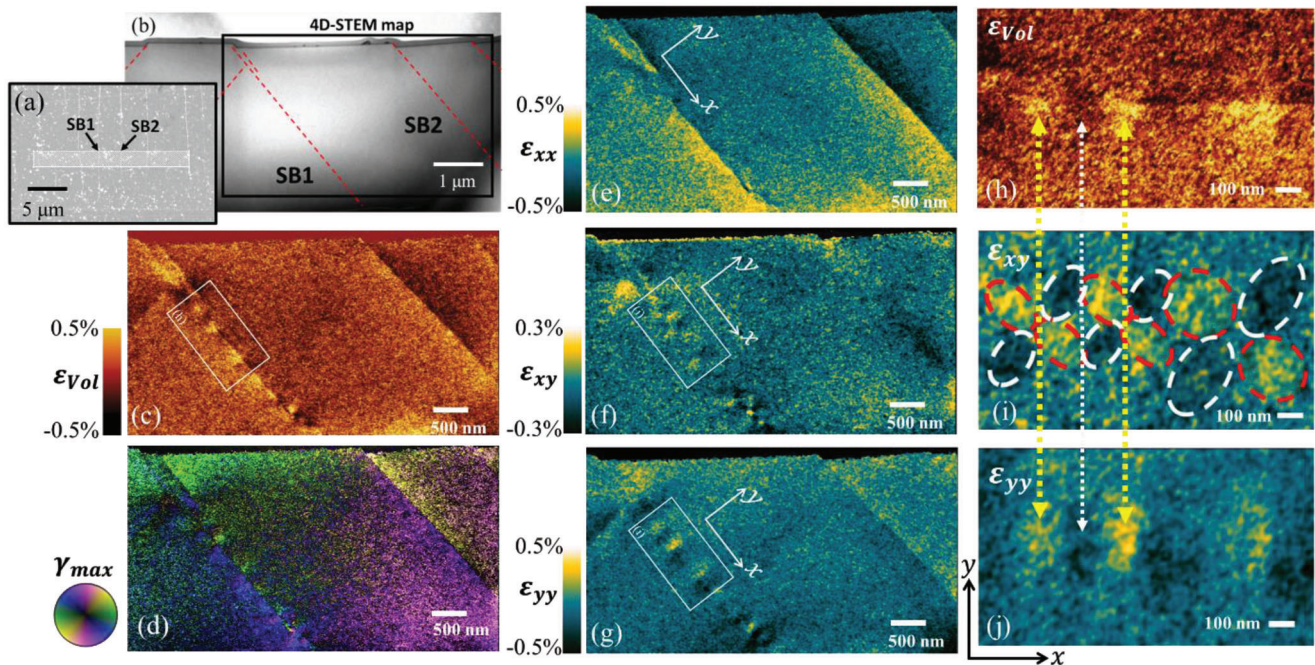


Figure 2. Deformed $\text{Fe}_{85.2}\text{Si}_{0.5}\text{B}_{9.5}\text{P}_4\text{Cu}_{0.8}$ metallic glass ribbon. a) SEM image showing the area beside a scratch with shear offsets clearly visible. The shadowed rectangle indicates the location of the prepared TEM lamella. b) STEM-HAADF image of the TEM lamella, where the expected locations of the shear bands are indicated by red dashed lines according to shear offset at the surface. A 4D-STEM map was acquired at the area indicated by the black rectangle, where the shear bands of interest are labeled as SB1 and SB2. c) Map of volumetric strain (ϵ_{Vol}). d) Map of maximum shear strain (γ_{max}). The color corresponds to the orientation, and the brightness corresponds to the amplitude, as indicated by the color wheel. For the strain tensors, the x -axis is defined to be parallel to SB1 and the y -axis perpendicular to SB1. e) ϵ_{xx} , the strain component along the x -axis, f) ϵ_{xy} , the shear component, and g) ϵ_{yy} , the strain component along the y -axis. h–j) show the correlation of ϵ_{Vol} , ϵ_{xy} , and ϵ_{yy} , which are magnified images of the area indicated by the white rectangles in (c), (f), and (g). The dashed ellipses indicate the quadrupole strain field. The yellow dashed arrows indicate the center of the quadrupoles.

information on local distortions without contributions from hydrostatic stress. The strain tensors obtained from the principal strains (Figure S2, Supporting Information) are shown in Figure 2e–g, where we defined the x -axis to be parallel to SB1 and the y -axis perpendicular to SB1 to visualize shear band features. The color code in ϵ_{xx} and ϵ_{yy} indicates the strain amplitude: dark-blue (negative sign) represents compression corresponding to atoms squeezed closer along the axial direction, whereas bright-yellow (positive sign) represents tension indicating an increased distance between atoms. The color code in ϵ_{xy} indicates shearing: positive values for clockwise shearing and negative ones for anticlockwise.

The strain maps, e.g. ϵ_{xx} (Figure 2e), reveal an asymmetric strain distribution across shear bands with a sharp transition (3 scanning steps) occurring at the shear plane. Considering the probe and scan step size, this provides an upper estimate of the projected width of the shear band to be about 15 nm. The asymmetric feature can be understood by the opposite motion of the material on each side of the shear band during deformation. Based on the shear offset, it can be confirmed that the pop-in side of the shear band is compressed and the opposite side is in tension. This matches the observations by Scudino et al.^[27] and Shahabi et al.^[28] using X-ray diffraction. However, complementary to the micrometer resolution of the X-ray based technique, the nanometer resolution in 4D-STEM reveals new details of the strain variation around the shear bands. ϵ_{xy} (Figure 2f) shows zig-zag arranged shear fields on SB1. ϵ_{yy} (Figure 2g) alternates

between tension and compression along SB1. These features can be understood better by the γ_{max} map (Figure 2d), where the orientation of the strain field circularly rotates along SB1. This coincides with alternating fluctuations along SB1 observed for the volumetric strain ϵ_{Vol} (Figure 2c). The enlarged areas indicated by the white rectangles in the ϵ_{Vol} , ϵ_{xy} , and ϵ_{yy} are shown in Figure 2h–j. Eshelby-like inclusions are observed along SB1. The ϵ_{xy} map reveals quadrupolar shear fields produced by the inclusions. Each of the quadrupoles consists of a positive pair (red dashed ellipse) and a negative pair (white dashed ellipse) perpendicular to each other and oriented $\approx 45^\circ$ to the shear band plane. The center of each quadrupole exhibits a volumetric expansion and strong tensile strain ϵ_{yy} as indicated by yellow-dashed arrows. Between the inclusions, compressive ϵ_{yy} and volumetric shrinkage are observed as indicated by a white-dashed arrow.

Besides SB1, we observed a different type of shear band, such as SB2, which exhibits negligible Eshelby-like features along the shear band but a stronger asymmetric strain with a ≈ 10 nm sharp transition across the shear plane, as shown in Figure S3 (Supporting Information).

To examine the details of the strain field at SB1, we plot the maximum shear strain (γ_{max}) as arrow-less vectors overlaid on the map of ϵ_{Vol} in Figure 3a. The length of the lines represents the strength of γ_{max} and the orientation indicates the maximum tensile direction. The black dashed rectangular area is magnified at the top of Figure 3b. We compare it with the quadrupolar features from the same area of the shear strain map (middle) and the

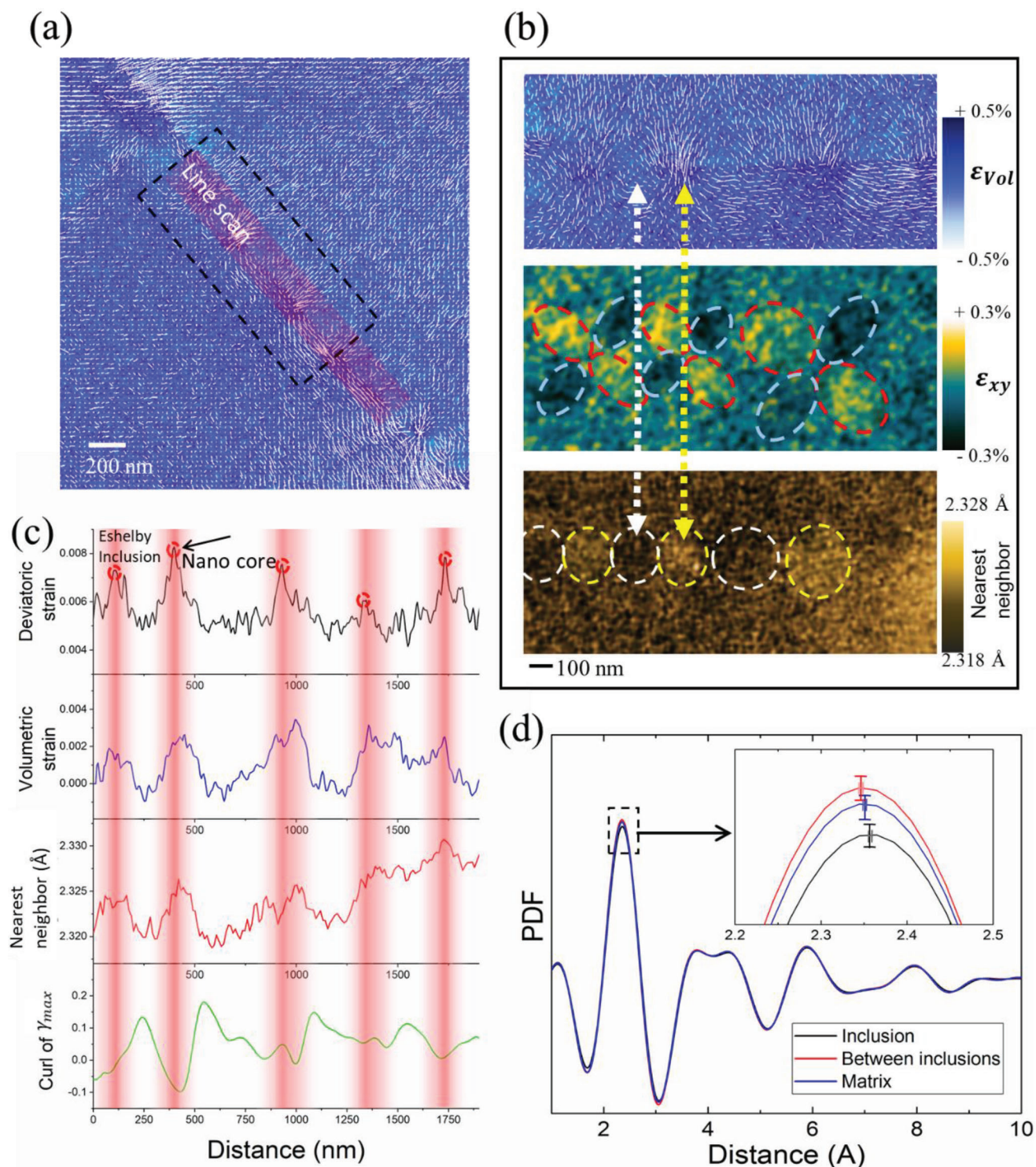


Figure 3. a) Vector field visualization of the maximum shear strain, γ_{max} , overlaid on the map of volumetric strain for $\text{Fe}_{85.2}\text{Si}_{0.5}\text{B}_{9.5}\text{P}_4\text{Cu}_{0.8}$. b) (top) Magnified region from the black rectangular area in (a) compared to maps of ϵ_{xy} and the nearest-neighbor distance from the same region. c) Line profiles of the deviatoric strain, volumetric strain, nearest-neighbor distance, and curl of γ_{max} along the shear band in the region indicated by a red rectangle in (a). The positions of the Eshelby inclusions and their nano core are highlighted by red gradient windows in (a). d) PDFs averaged from typical inclusions and in-between inclusions marked by white and yellow dashed circles in Figure 3b (bottom) together with a PDF of the matrix taken from an area away from the quadrupoles. The error bars (standard deviation) are estimated based on the observed variations in 2500 PDFs taken from an undeformed region.

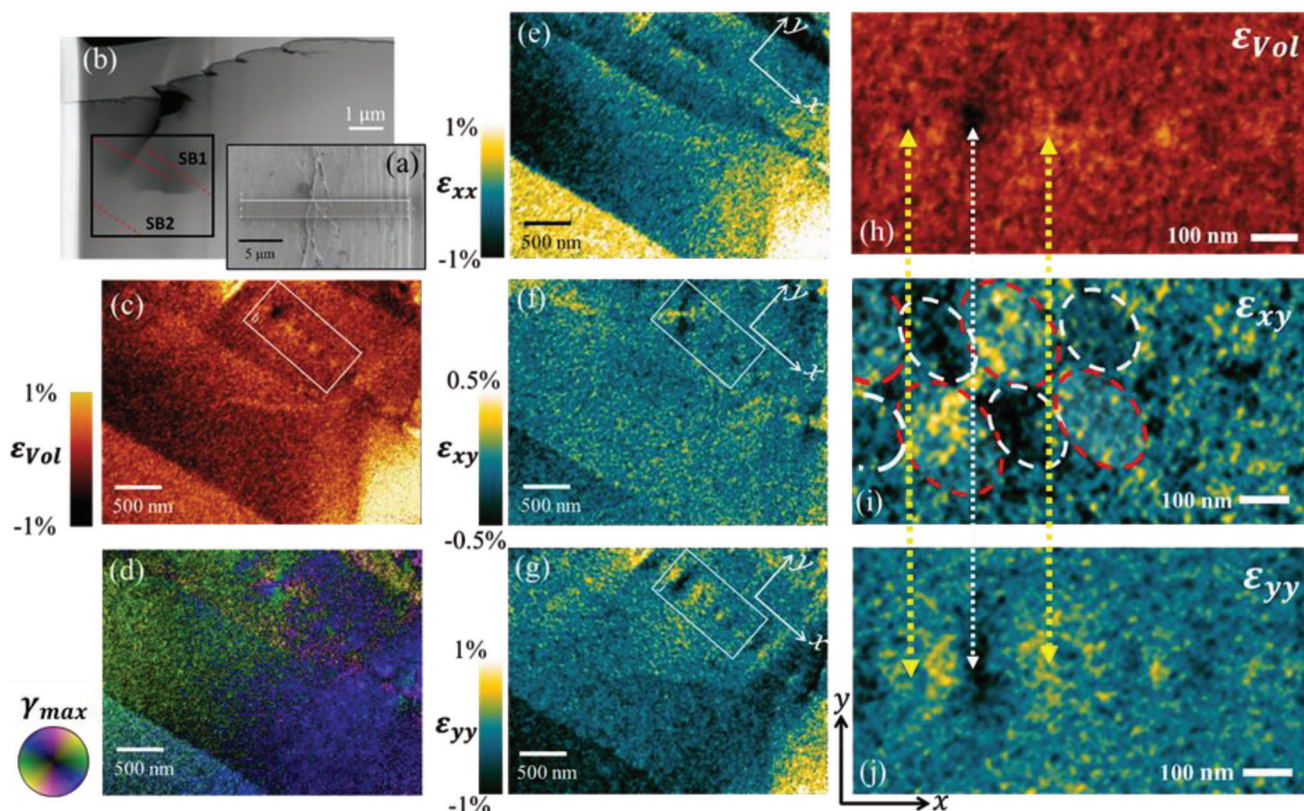


Figure 4. Deformed $Zr_{46}Cu_{38}Al_8Ag_8$ bulk metallic glass. a) SEM image showing the area beside a scratch with shear offsets and microcracks. The shadowed rectangle indicates the location of the TEM lamella. b) STEM-HAADF image of the TEM lamella, where the location of shear bands is indicated by red dashed lines. A 4D-STEM map was acquired at the area indicated by the black rectangle, where the shear bands of interest are labeled as SB1 and SB2. c) Map of volumetric strain (ϵ_{Vol}). d) Map of maximum shear strain (γ_{max}). The color corresponds to the orientation of γ_{max} and the brightness to the amplitude as indicated by the color wheel. For the strain tensors, the x -axis is defined to be parallel to SB1 and the y -axis perpendicular to SB1. e) ϵ_{xx} , the strain tensor component along the x -axis, f) ϵ_{xy} , the shear component, and g) ϵ_{yy} , along the y -axis. h–j) show the correlation between the strain components and ϵ_{Vol} , which are magnified images of the area indicated by the white rectangles in (c), (e), and (g). The dashed ellipses indicate the quadrupole strain field. The yellow dashed arrows indicate the centers of the quadrupole strain fields.

map of the nearest-neighbor distance obtained from STEM-PDF (bottom, the full map can be seen in Figure S4a, Supporting Information). It can be seen that the strain concentrates at the core of inclusions located at the center of the quadrupoles with a larger nearest-neighbor atomic distance. The strain fields extend from the core in a circular way toward the adjacent inclusions forming a vortex-like rotation field in between.

In Figure 3c, we quantified the maps of the deviatoric, volumetric strain, and atomic nearest-neighbor distance as well as the curvature (curl) of the rotational γ_{max} field by line profiles along SB1. The maxima of the deviatoric strain, where the materials suffer the strongest shear transformation, coincide with the maxima of the volumetric strain and the enlarged nearest-neighbor atomic distance. The inclusions are separated by regions with a high curl of γ_{max} , weak deviatoric, and volumetric strain, where atoms are arranged with a smaller 1st coordination shell. The stress field concentrated around the inclusion influences the surrounding material and fades only gradually, making it difficult to experimentally define the real size of the core of the inclusions. Nevertheless, it is worth noting that the deviatoric strain (Figure 3c, black line), which disentangles the true material distortion from the volumetric change, exhibits

remarkably sharp maxima with a size of about 15 nm (≈ 3 scanning steps).

Figure 3d shows PDFs averaged from dashed circular areas marked in Figure 3b (bottom) for a typical inclusion, in-between inclusions and the matrix away from the quadrupoles. No significant differences among the PDFs can be observed, except a statistically meaningful shift toward a larger distance of the 1st peak and a reduced height of the peak from the inclusions compared to the compressed area in-between inclusions and the matrix away from the shear band. Together with the volumetric strain, this observation supports the conclusion that the hydrostatic stress surrounding the inclusions increases the average atomic distance and dilates the material at the inclusions.

To confirm the universality of the phenomenon, we applied our 4D-STEM approach to a $Zr_{46}Cu_{38}Al_8Ag_8$ (at.%) bulk metallic glass, which possesses mechanical properties distinct from the Fe-based metallic glass. Figure 4a shows a scratched surface of the metallic glass. A TEM sample including the pile-up area was prepared from the area indicated by the shadowed rectangle. A 4D-STEM map was acquired below the deformed surface in the area indicated by the black rectangle in Figure 4b, where the shear bands of interest are labeled as SB1 and SB2.

Figure 4c,d shows maps of ϵ_{Vol} and γ_{max} . The strain tensors obtained from the principal strains (Figure S5, Supporting Information) are shown in Figure 4e–g, where the x -axis is parallel to SB1 and the y -axis is perpendicular to SB1. The results show qualitatively the same phenomena as observed in the Fe-based metallic glass. Again, two types of shear bands are observed. For SB1, we see quadrupolar strain fields concentrated at the dilated inclusions (Figure 4h–j). SB2 exhibits negligible variation along the shear band but a stronger asymmetric strain variation across the shear band. The features observed in the Cu–Zr based metallic glasses are weaker compared to the Fe-based sample. This may be due to the softer nature of the Cu–Zr-based glasses.^[29–31] The soft Cu–Zr-based glass possesses more intrinsic structural inhomogeneity compared to the rigid Fe-based glasses, giving rise to a higher noise-like background in the maps, which has also been observed by Gammer et al.^[24] Furthermore, the stress built up during deformation relaxes easily in soft glass, leading to weaker residual features. Nevertheless, the quadrupolar features and the dilated inclusions can be confirmed (as shown in Figure 4i and Figure S6, Supporting Information).

2. Discussion

According to Eshelby's theory, the inclusions can be quantified as plastic zones at the core of the quadrupoles, where the material's elasticity is changed due to the plastic event.^[32] In our observation, the preserved "quadrupole strain fields", which are concentrated around the core of the inclusion, influence the surrounding material and fade only gradually, making it difficult to experimentally define the real size of the core of the inclusions. Nevertheless, the sharp concentration of the deviatoric strain indicates that plastic deformation occurred at the core of the observed inclusions, enabling us to estimate an upper limit for the size of the inclusion with a diameter of less than about 15 nm. A question naturally arises here: what are the inclusions observed in SB1? The formation of a shear band is believed to be initiated by the activation of shear transformation zones (STZs).^[5] Atomistic modeling proposed STZs to be Eshelby inclusions, where atoms suffer plastic displacements,^[6,7] resulting in significant atomic dilatation^[33–35] and a shear stress field with quadrupolar symmetry.^[8,9,36] The quadrupolar stress field perturbs the surrounding atoms to a vortex-like motion and percolates the inclusions eventually leading to the formation of a shear band.^[35,37–39] Yang et al. disentangled the localized dilatation from the shear strain and rotation in the atomic scale modeling and proposed that Eshelby inclusions are initialized from the dilatation process followed by the secondary activation of rotation in neighboring hard material, which excellently matches to our observation.^[35] Simulations have suggested two possible scenarios for the motions of the inclusions: the plastic zones behave in a synchronized fashion and the emergence of the shear band occurs in a directly percolated manner,^[40,41] or the structural perturbation, generated by the stress concentration at the leading inclusion, triggers the activation of neighboring inclusions via rotational shear fields leading to an autocatalytic propagation of the shear band.^[39] Experimentally, such vortex-like perturbations have been reported in condensed granular colloids and originated from the interaction of STZs through the stress mediated by the rigid surrounding material.^[42,43] In all these works, the observed topol-

ogy of STZs was analogous to our observations. However, the STZ event is believed to be a transient phenomenon and our observations correspond to a static measurement of the residual stress and structural changes after the plastic deformation. Furthermore, the size of the inclusion cores we observed is about 10 times larger than the size of a STZ usually observed in atomic modeling.^[6,37,44] Therefore, it is hard to directly relate the observed inclusions to individual STZ events.

The obvious next question is what are the observed structures if they are not STZs? Such strain fields with quadrupolar symmetry were also observed at ≈ 10 nm voids in a simulated metallic glass by molecular dynamics (MD) simulations^[45] and also at a ≈ 1 mm void in a lab-prepared metallic glass using X-ray diffraction under load.^[23] According to continuum mechanics, the concentration of quadrupolar stresses is a universal phenomenon across different length scales at Eshelby inclusions during loading.^[32] One potential explanation is that the continuous creation of STZ events followed by their agglomeration can form such plastic zones. Very recently, Sheng et al. associated a nanoscale density map from a 4D-STEM experiment with MD simulation and predicted the formation of such Eshelby-like strain concentration along the shear front in a metallic glass.^[46] The resulting plastically deformed zones concentrate the stress. The concentrated stress perturbs the surrounding material in a vortex-like manner and percolates the neighboring inclusions. This eventually leads to the formation of a shear band.

The observation of two different types of shear bands may result from a hypothesis: SB1 has suffered limited shear displacement preserving the Eshelby-like features compared to the more mature SB2. It is worth noting that SB2 exhibits weak but detectable fluctuations along the shear band with a similar length as in SB1 as shown by the red line profile in Figure S3b (Supporting Information). This hints that SB1 and SB2 have certain similarities and could be originated from the same mechanism. Such a hypothesis has also been suggested in atomic level simulations, where quadrupolar stress features, formed during the initiation of a shear band (SB1-like), are later on smeared out during the shear displacement, giving rise to a more homogeneous linear band structure (SB2-like).^[9,39] However, we noticed that there are large strain variations, e.g. deviatoric strain up to 0.5% and volumetric strain up to 1%, observed at a projected core of inclusion with a diameter of a few tens of nanometers. Considering that we are looking at a projection averaging across the sample thickness, the observed large strain could hardly be physically reasonable for a 200–250 nm thick sample if the inclusion core is a pointlike 0D structure. This could lead to speculation that the inclusion is a tubular structure extending in and out of the imaging page. In this case, the shear band can appear differently when they have large misorientation between each other in the sample. Given the limitation of postmortem characterization and 2D projection of the strain field in the 3D volume, our experiment cannot conclusively explain why SB2 is different from SB1. Nevertheless, the observation of the two types of shear bands in identical samples nicely explains the distinct differences among STEM observations of shear bands, e.g. Rösner et al. observed shear bands showing alternating STEM-ADF contrast,^[11,12] whereas Maaß et al. showed shear bands simply exhibiting a reduced intensity^[10] as well as the previous observation of an asymmetric variation of the interatomic distances across

shear bands.^[47] The results also confirm the hypothesis of Eshelby quadrupole alignment along shear bands by Hieronymus-Schmidt et al.^[48]

In summary, the correlative strain field and atomic PDF mapping demonstrate a new approach to obtain crucial information for studying deformation mechanisms in metallic glasses. It provides for the first time an experimental visualization of the Eshelby inclusions surrounded by quadrupolar strain fields aligned on a shear band in deformed metallic glasses. Examination of the two distinct metallic glasses suggests the universality of our observation. The results provide direct experimental evidence for a concrete scenario for the initiation of a shear band: the dilated Eshelby inclusions are the result of local plastic atomic displacements in the glassy matrix, which concentrate a stress field with quadrupolar symmetry. The quadrupolar stress field perturbs the surrounding material in a vortex-like manner and percolates neighboring inclusions. This eventually leads to the formation of a shear band. Our new method is expected to initiate broad research possibilities for solving questions in amorphous matters.

3. Experimental Section

Fe_{85.2}Si_{0.5}B_{9.5}P₄Cu_{0.8} (at.%) and Zr₄₆Cu₃₈Al₈Ag₈ (at.%) master alloy ingots were prepared by arc melting in a Ti-gettered argon atmosphere. The Fe_{85.2}Si_{0.5}B_{9.5}P₄Cu_{0.8} (at.%) ribbons, width ≈ 25 mm and thickness ≈ 20 μm, were prepared from the melt by rapid solidification onto rotating Cu wheels. The Zr₄₆Cu₃₈Al₈Ag₈ bulk metallic glass (1 cm × 1 cm × 1 mm plate) was fabricated by suction-casting into a water-cooled copper mold. The amorphous nature of samples was confirmed by X-ray diffraction (XRD), electron diffraction as well as differential scanning calorimetry (DSC).

Scratch tests were performed with a scratch length $l_s = 1$ mm with normal loads $F_n = 10$ N for the Fe-based metallic glass ribbon and $F_n = 15$ N for the Cu–Zr-based bulk metallic glass with a sliding velocity versus = 0.1 mm s⁻¹ under ambient conditions using a diamond tip with a radius of 210 μm. For the STEM analysis, electron transparent TEM lamellae were prepared by focused ion beam (FIB), FEI Strata 400S, lifting out a specimen from the vicinity of the scratches. Thinning was performed in the FIB at an acceleration voltage of 30 kV with gradually decreasing beam currents from 2 nA to 8 pA to reduce the ion beam damage. A lamella thickness of ≈200 nm was obtained to balance electron transparency and prevent strain relaxation due to an enlarged surface-to-volume ratio (Figure S7, Supporting Information).

4D-STEM measurements were conducted using a Themis Z double-corrected TEM (ThermoFisher Scientific) operated at 300 kV in microprobe STEM mode with spot size 6 and a semi-convergence angle of 0.26 mrad giving rise to a diffraction-limited probe size of ≈5 nm. 4D-STEM recorded local 2D diffraction patterns over a 2D array of probe positions by stepwise scanning of the probe. The method was called 4D-STEM referring to its typical 4D dataset (2D diffraction pattern on a 2D array of the sample). A OneView camera (Gatan Inc.) was used with a camera length of 1.15 m to record the diffraction patterns. This camera length was chosen to capture the first diffuse diffraction ring with a sufficient diameter on the camera to enhance the sensitivity for measuring distortions. The 2nd diffuse diffraction ring was also included. This preserved the capability for PDF analysis. 4D-STEM maps were acquired with a step size of 5.8 nm and a frame size of 900 × 500 pixels for the Fe_{85.2}Si_{0.5}B_{9.5}P₄Cu_{0.8} metallic glass ribbon and a step size of 9.7 nm and a frame size of 350 × 270 pixels for the Zr₄₆Cu₃₈Al₈Ag₈ bulk metallic glass with an exposure time of 3.3 ms per frame (frame rate of ≈300 f s⁻¹).

The diffraction pattern of a typical amorphous material showed a diffuse ring pattern (Figure 1a). As described in previous works,^[23–24,27] the

local stress in the metallic glass induced a structural anisotropy, which resulted in an elliptic distortion of the diffraction ring leading to a deviation from the ideal circle as illustrated in Figure 1b (the diffraction pattern was artificially elongated for easy presentation). Therefore, the strain could be mapped by determining the ellipticity of the diffraction ring in each local diffraction pattern of the 4D-STEM dataset. Different from high-resolution (HR)TEM-based strain mapping methods such as geometric phase analysis (GPA), which analyzed real space atomic lattice displacements,^[49] the strain measurement used here analyzed the diffraction ring in the 4D-STEM data. It thus enabled the capability to measure strain for amorphous materials and a large field of view (up to micrometers).

An algebraic method was adopted using singular value decomposition (SVD) proposed by Fitzgibbon et al.^[50] to fit an ellipse to the diffraction ring. This provided an unbiased fitting method with high precision and orders of magnitude reduced demand for computational power compared to non-linear or iterative fitting methods. The diffraction patterns were first binarized by applying a threshold: Intensity = 1 when $0.95I_{\max} < I(q_x, q_y) < I_{\max}$ and Intensity = 0 everywhere else, where I_{\max} is maximum intensity in the diffraction pattern and q_x and q_y are the coordinates of the pixels in reciprocal space. An ellipse in the reciprocal space can be represented by an implicit second-order polynomial equation:

$$F(C, Q) = C \cdot Q = aq_x^2 + bq_xq_y + cq_y^2 + dq_x + eq_y + f \quad (1)$$

where $C = [a \ b \ c \ d \ e \ f]$ and $Q = [q_x^2 \ q_xq_y \ q_y^2 \ q_x \ q_y \ 1]^T$. $F(C, Q)$ is the mismatch distance of a data point (q_x, q_y) to the ellipse $F(C, Q) = 0$. Thus, the best fit of an ellipse to the diffraction ring is equivalent to finding C to minimize

$$D(C) = \min \sum_{i=1}^N F(C, Q_i)^2,$$

where N is the total number of selected pixels by the thresholding and i is the pixel sequence number. This least square problem can be solved by singular value decomposition (SVD) considering a rank-deficient generalized eigenvalue system, as $QQ^T C^T = \lambda PC^T$, where P is a constrain matrix to avoid trivial solutions, e.g., $C = 0$, as defined by

$$P = \begin{bmatrix} 0 & 0 & -2 & 0 & 0 & 0 \\ 0 & 1 & 0 & 0 & 0 & 0 \\ -2 & 0 & 0 & 0 & 0 & 0 \\ 0 & 0 & 0 & 0 & 0 & 0 \\ 0 & 0 & 0 & 0 & 0 & 0 \\ 0 & 0 & 0 & 0 & 0 & 0 \end{bmatrix} \quad (2)$$

Solving the eigenproblem produces six eigenvalues and eigenvectors. The eigenvector associated with the smallest eigenvalue was the C component minimizing the sum of squared mismatch distances, which was equivalent to the linear least square fitting method. Note that the center position of the diffraction patterns could shift when scanning a large field of view due to the distortion of the beam-focusing lens. The fitting algorithm simultaneously tracked the centers of the individual diffraction patterns for accurate fitting. From the fitted ellipse,

the principal strains were determined as $\bar{P}_1 = \frac{q_0 - q_{\max}}{q_0} \begin{pmatrix} \cos(\theta) \\ \sin(\theta) \end{pmatrix}$ and

$\bar{P}_2 = \frac{q_0 - q_{\min}}{q_0} \begin{pmatrix} \cos(\theta + 90^\circ) \\ \sin(\theta + 90^\circ) \end{pmatrix}$, where q_0 is the radius of the 1st ring for the unstrained case (averaged from an area far away from the deformed region), q_{\max} , and q_{\min} are the length of the maximum and minimum elliptical axis of the 1st ring. θ is the corresponding azimuthal angle of q_{\max}

to the x-axis. The deviatoric strain was calculated as $\epsilon_{\text{dev}} = \frac{|\bar{P}_1| - |\bar{P}_2|}{2}$.

The volumetric strain was calculated as $\epsilon_{\text{vol}} = \frac{|\bar{P}_1| + |\bar{P}_2|}{2}$. Strain tensors were calculated by setting the coordinate system with the x-axis parallel to the shear band of interest and the y-axis perpendicular to the shear

band as $\begin{pmatrix} \epsilon_{xx} & \epsilon_{xy} \\ \epsilon_{yx} & \epsilon_{yy} \end{pmatrix} = \mathbf{R} \begin{pmatrix} |\bar{P}_1| & 0 \\ 0 & |\bar{P}_2| \end{pmatrix} \mathbf{R}^T$, where $\mathbf{R} = \begin{pmatrix} \cos(\theta) & -\sin(\theta) \\ \sin(\theta) & \cos(\theta) \end{pmatrix}$ is a rotation matrix. ϵ_{xx} and ϵ_{yy} represented the strain along the x-axis and y-axis. A positive value meant tensile strain indicating the atoms were

pulled away from each other and a negative value indicated compressive strain corresponding to atoms squeezed closer along the axial direction. ϵ_{xy} represented the shear component of the strain tensor. A positive value indicated the clockwise and a negative value for anticlockwise shearing. The maximum shear strain was determined as

$$\gamma_{\max} = \frac{|\bar{P}_1| - |\bar{P}_2|}{2} \begin{pmatrix} \cos(\theta) \\ \sin(\theta) \end{pmatrix}. \text{ The amplitude was defined as deviatoric}$$

strain and the orientation indicates the maximum tensile direction. The curl of the maximum shear strain was calculated using the Matlab built-in function “curl(γ_{\max})”. Although multiple scattering occurred in the thick sample, which reduced the intensity of the diffraction rings and reduced the signal-to-noise level, the intensity of the 1st ring was sufficient for the fitting algorithm. Multiple scattering was an azimuthally isotropic process in amorphous materials within the sampling volume of the experiment. Therefore, it did not create an artificial anisotropy of the diffraction ring. For clarification, the effect of thickness on the radius of the diffraction ring (taken from an unstrained area) was checked as shown in Figure S8 (Supporting Information). It showed that changes in thickness from 70 to 200 nm lead to variations of less than 0.02% of the peak position, which was more than 20 times smaller than the volumetric strain variation at the SBs ($\approx 0.4\%$). All this guaranteed confidence in the measurement for thick samples. The accuracy of the strain measurements was further examined by mapping the squared mismatch distances (fitting error) for fitting every diffraction pattern and compared with the map of the 1st ring radius in Figure S9 (Supporting Information). Random noise was only observed in the error map with a standard deviation of $0.000607 \text{ \AA}^{-1}$ (Figure S9a, Supporting Information). For comparison, the map of the 1st ring radius showed clear shear band features (Figure S9b, Supporting Information), e.g., an asymmetric distribution across the shear bands and alternating fluctuations along the shear band. In addition, the standard deviation of volumetric strain was calculated using the data acquired far away from the shear bands (less strained) to be 0.08%. Gammer et al reported that this estimation was also affected by the local structural variations, which intrinsically existed in the metallic glasses. Therefore, this standard deviation was an upper limit for the uncertainty of the strain measurement.^[24] Nevertheless, the small standard deviation was well below the typical shear band features ($>0.2\text{--}0.5\%$) in the experimental observation.

For STEM-PDF analysis, the processes followed were described in Ref. [21,22]. The diffraction patterns were integrated azimuthally to obtain radius profiles $I(q)$, where $q = 2\theta/\lambda$, θ is half of the scattering angle, and λ is the incident wavelength. The azimuthal integration helped to obtain a high signal-to-noise ratio at large scattering angles. The structure factor (Figure 1b, bottom left) was calculated by subtracting and normalizing with single atomic scattering factors according to $S(q) = \frac{I(q) - N\langle f(q)^2 \rangle}{N\langle f(q)^2 \rangle} q$, where N is the number of atoms within the volume sampled by the electron probe, $f(q)$ is the parameterized electron scattering factors for a single atom, calculated based on Ref. [51], $\langle f(q) \rangle = \sum_i C_i f_i(q)$ denotes

an elemental average of the atomic scattering factor $f_i(q)$ over all elements, C_i presents in the atomic percentage of the i^{th} element. The PDFs (Figure 1b, bottom right) were obtained by a Fourier sine transformation

$$\text{of the structure factors according to PDF}(r) = \int_0^{q_{\max}} S(q) \sin(2\pi qr) dq. \text{ The}$$

only adjustable parameter in the PDF calculation was N , which was determined for each PDF in the map by minimizing $S(q)$ to approach zero at large q . This reduced effects caused by variations in thickness \times atomic density in the samples. A smooth 4th-order polynomial function was subtracted from the structure factor to reduce the effect caused by multiple scattering and contributions from inelastic scattering.^[21] A relatively large camera length (resulting in a limited k range) was used to capture the first diffraction ring with a sufficient diameter on the camera to enhance the sensitivity for measuring the distortions. The limited k range could cause a broadening of PDF peaks due to the truncation of high-frequency information in the reciprocal space. However, it did not alter peak positions (see Figure S10, Supporting Information).^[52] The atomic nearest-neighbor distances were analyzed by fitting a Gaussian function to the 1st PDF peak. A slight gradual background change over micrometers could be observed in the nearest-neighbor map following the changes in the sample thickness

map (Figure S4b, Supporting Information). This was because of the strong multiple scattering broadening peaks in $S(q)$, which slightly shifted the peak position in the PDF toward shorter distances with increasing thickness. However, the gradual background changes did not affect the observation of the nanometer scale local deformation features near the shear bands (Figure S4c, Supporting Information).

Supporting Information

Supporting Information is available from the Wiley Online Library or from the author.

Acknowledgements

The authors are grateful to the Karlsruhe Nano Micro Facility (KNMF) for support and access to FIB and TEM facilities. X.M. acknowledges the financial support received from Deutsche Forschungsgemeinschaft's (DFG) funding (MU 4276/1-1)

Open access funding enabled and organized by Projekt DEAL.

Conflict of Interest

The authors declare no conflict of interest.

Author Contributions

S.K. and X.M. developed the methods and performed TEM experiments. K.D. and C.M. provided the Fe-based sample. A.C. provided the Zr-based sample. S.K. and A.C. performed the deformation experiments. S.K., X.M., D.W., and C.K. analyzed the data. X.M. and C.K. supervised the project. S.K., X.M., and C.K. wrote the manuscript. All authors contributed to the revision of the manuscript.

Data Availability Statement

The data that support the findings of this study are openly available in KITOpen at <https://doi.org/10.5445/IR/1000157911>, reference number 1000157911.

Keywords

4D-STEM, Eshelby inclusions, metallic glass, shear bands, strain fields

Received: December 24, 2022

Revised: March 29, 2023

Published online: April 29, 2023

- [1] A. L. Greer, *Science* **1995**, 267, 1947.
- [2] M. Telford, *Mater. Today* **2004**, 7, 36.
- [3] C. A. Schuh, T. C. Hufnagel, U. Ramamurty, *Acta Mater.* **2007**, 55, 4067.
- [4] A. Greer, Y. Cheng, E. Ma, *Mater. Sci. Eng., R* **2013**, 74, 71.
- [5] Y. Cheng, E. Ma, *Prog. Mater. Sci.* **2011**, 56, 379.
- [6] H. Peng, M. Li, W. Wang, *Phys. Rev. Lett.* **2011**, 106, 135503.
- [7] J. Ding, S. Patinet, M. L. Falk, Y. Cheng, E. Ma, *Proc. Natl. Acad. Sci. USA* **2014**, 111, 14052.

- [8] D. Şopu, X. Yuan, F. Moitzl, F. Spieckermann, X. Bian, J. Eckert, *Appl. Mater. Today* **2021**, 22, 100958.
- [9] R. Dasgupta, H. G. E. Hentschel, I. Procaccia, *Phys. Rev. E* **2013**, 87, 022810.
- [10] C. Liu, V. Roddatis, P. Kenesei, R. Maaß, *Acta Mater.* **2017**, 140, 206.
- [11] H. Rösner, M. Peterlechner, C. Kübel, V. Schmidt, G. Wilde, *Ultramicroscopy* **2014**, 142, 1.
- [12] V. Schmidt, H. Rösner, M. Peterlechner, G. Wilde, P. M. Voyles, *Phys. Rev. Lett.* **2015**, 115, 035501.
- [13] S. Balachandran, J. Orava, M. Köhler, A. J. Breen, I. Kaban, D. Raabe, M. Herbig, *Scr. Mater.* **2019**, 168, 14.
- [14] D. Louzguine-Luzgin, A. Trifonov, Y. P. Ivanov, A. Lu, A. Lubenchenko, A. Greer, *Sci. Rep.* **2021**, 11, 13650.
- [15] M. Chen, A. Inoue, W. Zhang, T. Sakurai, *Phys. Rev. Lett.* **2006**, 96, 245502.
- [16] Z. Yan, K. Song, Y. Hu, F. Dai, Z. Chu, J. Eckert, *Sci. Rep.* **2016**, 6, 19358.
- [17] F. Zhu, S. Song, K. M. Reddy, A. Hirata, M. Chen, *Nat. Commun.* **2018**, 9, 3965.
- [18] A. Liu, R. Tabor, L. Bourgeois, M. De Jonge, S. Mudie, T. Petersen, *Phys. Rev. Lett.* **2016**, 116, 205501.
- [19] F. Zhu, A. Hirata, P. Liu, S. Song, Y. Tian, J. Han, T. Fujita, M. Chen, *Phys. Rev. Lett.* **2017**, 119, 215501.
- [20] J. Hwang, P. Voyles, *Microsc. Microanal.* **2011**, 17, 67.
- [21] X. Mu, D. Wang, T. Feng, C. Kübel, *Ultramicroscopy* **2016**, 168, 1.
- [22] X. Mu, A. Mazilkin, C. Sprau, A. Colsmann, C. Kübel, *Microscopy* **2019**, 68, 301.
- [23] H. F. Poulsen, J. A. Wert, J. Neufeind, V. Honkimäki, M. Daymond, *Nat. Mater.* **2005**, 4, 33.
- [24] C. Gammer, C. Ophus, T. C. Pekin, J. Eckert, A. M. Minor, *Appl. Phys. Lett.* **2018**, 112, 171905.
- [25] W. Dmowski, T. Iwashita, C.-P. Chuang, J. Almer, T. Egami, *Phys. Rev. Lett.* **2010**, 105, 205502.
- [26] M. Kuhnt, M. Marsilius, T. Strache, C. Polak, G. Herzer, *Scr. Mater.* **2017**, 130, 46.
- [27] S. Scudino, D. Şopu, *Nano Lett.* **2018**, 18, 1221.
- [28] H. S. Shahabi, S. Scudino, I. Kaban, M. Stoica, B. Escher, S. Menzel, G. B. Vaughan, U. Kühn, J. Eckert, *Acta Mater.* **2016**, 111, 187.
- [29] C. Suryanarayana, A. Inoue, *Bulk Metallic Glasses*, CRC Press, Boca Raton, FL, USA **2017**.
- [30] J. Schroers, W. L. Johnson, *Phys. Rev. Lett.* **2004**, 93, 255506.
- [31] Y. H. Liu, G. Wang, R. J. Wang, D. Q. Zhao, M. X. Pan, W. H. Wang, *Science* **2007**, 315, 1385.
- [32] J. D. Eshelby, *Proc. R. Soc. London, Ser. A* **1957**, 241, 376.
- [33] M. Jiang, G. Wilde, L. Dai, *Scr. Mater.* **2017**, 127, 54.
- [34] J. Pan, Q. Chen, L. Liu, Y. Li, *Acta Mater.* **2011**, 59, 5146.
- [35] Z.-Y. Yang, Y.-J. Wang, L.-H. Dai, *Phys. Rev. Res.* **2022**, 4, 023220.
- [36] R.-H. Shi, Y.-C. Wu, F. Shuang, Z.-W. Zhang, *Mater. Today Commun.* **2023**, 34, 105389.
- [37] X. Bian, D. Şopu, G. Wang, B. Sun, J. Bednarčík, C. Gammer, Q. Zhai, J. Eckert, *NPG Asia Mater.* **2020**, 12, 59.
- [38] D. Şopu, S. Scudino, X. Bian, C. Gammer, J. Eckert, *Scr. Mater.* **2020**, 178, 57.
- [39] D. Şopu, A. Stukowski, M. Stoica, S. Scudino, *Phys. Rev. Lett.* **2017**, 119, 195503.
- [40] A. Cao, Y. Cheng, E. Ma, *Acta Mater.* **2009**, 57, 5146.
- [41] G. P. Shrivastav, P. Chaudhuri, J. Horbach, *Phys. Rev. E* **2016**, 94, 042605.
- [42] J. M. Paddidri, C. M. Hansen, S. D. Mesarovic, B. Muhunthan, *J. Appl. Mech.* **2012**, 79, 031011.
- [43] P. Schall, D. A. Weitz, F. Spaepen, *Science* **2007**, 318, 1895.
- [44] T. C. Hufnagel, C. A. Schuh, M. L. Falk, *Acta Mater.* **2016**, 109, 375.
- [45] P. Wen, B. Demaske, S. R. Phillpot, D. E. Spearot, G. Tao, S. Yuan, *J. Appl. Phys.* **2019**, 125, 133302.
- [46] H. Sheng, D. Şopu, S. Fellner, J. Eckert, C. Gammer, *Phys. Rev. Lett.* **2022**, 128, 245501.
- [47] X. Mu, M. R. Chellali, E. Boltynjuk, D. Gunderov, R. Z. Valiev, H. Hahn, C. Kübel, Y. Ivanisenko, L. Velasco, *Adv. Mater.* **2021**, 33, 2007267.
- [48] V. Hieronymus-Schmidt, H. Rösner, G. Wilde, A. Zaccone, *Phys. Rev. B* **2017**, 95, 134111.
- [49] M. J. Hÿtch, E. Snoeck, R. Kilaas, *Ultramicroscopy* **1998**, 74, 131.
- [50] A. Fitzgibbon, M. Pilu, R. B. Fisher, *IEEE Trans. Pattern Anal. Mach. Intell.* **1999**, 21, 476.
- [51] E. J. Kirkland, *Advanced Computing in Electron Microscopy*, Springer, New York **1998**.
- [52] J. Donohue, S. E. Zeltmann, K. C. Bustillo, B. Savitzky, M. A. Jones, G. F. Meyers, C. Ophus, A. M. Minor, *iScience* **2022**, 25, 103882.